Title

Photoinduced Charge Carrier Dynamics and Electron Injection Efficiencies in Au Nanoparticle-Sensitized TiO2 Determined with Picosecond Time-Resolved X-ray Photoelectron Spectroscopy

Journal

The Journal of Physical Chemistry Letters, 11(14)

ISSN

1948-7185

Authors

Borgwardt, Mario

Mahl, Johannes

Roth, Friedrich

et al.

Publication Date

2020-07-16

DOI

10.1021/acs.jpclett.0c00825

Peer reviewed

Photoinduced Charge Carrier Dynamics and Electron Injection Efficiencies in Au Nanoparticle-Sensitized TiO_2 Determined with Picosecond Time-Resolved X-ray Photoelectron Spectroscopy

Mario Borgwardt[1], Johannes Mahl[1], Friedrich Roth[2], Lukas Wenthaus[3], Felix Braußе[1], Monika Blum[1,4], Klaus Schwarzburg[5], Guiji Liu[1,6], Francesca M. Toma[1,6], and Oliver Gessner[1]*

[1]Chemical Sciences Division, Lawrence Berkeley National Laboratory, Berkeley, California 94720, USA

[2]Institute of Experimental Physics, TU Bergakademie Freiberg, D-09599 Freiberg, Germany

[3]Deutsches Elektronen Synchrotron / DESY, D-22607 Hamburg, Germany

[4]Advanced Light Source, Lawrence Berkeley National Laboratory, Berkeley, California 94720, United States

[5]Institute for Solar Fuels, Helmholtz-Zentrum Berlin für Materialien und Energie GmbH, 14109, Berlin, Germany

[6]Joint Center for Artificial Photosynthesis, Lawrence Berkeley National Laboratory, California 94720, USA

*corresponding author: ogessner@lbl.gov

Abstract

Progress in the development of plasmon-enabled light-harvesting technologies requires a better understanding of their fundamental operating principles and current limitations. Here, we employ picosecond time-resolved X-ray photoemission spectroscopy to investigate photoinduced electron transfer in a plasmonic model system composed of 20 nm sized gold nanoparticles (NPs) attached to a nanoporous film of TiO_2. The measurement provides direct, quantitative access to transient local charge distributions from the perspectives of the electron donor (AuNP) and the electron acceptor (TiO_2). On average, approximately two electrons are injected per NP, corresponding to an electron injection yield per absorbed photon of 0.1%. Back electron transfer from the perspective of the electron donor is dominated by a fast recombination channel proceeding on a timescale of 60±10 ps and a minor contribution that is completed after ≈1 ns. The findings provide a detailed picture of photoinduced charge carrier generation in this NP-semiconductor junction, with important implications for understanding achievable overall photon-to-charge conversion efficiencies.

TOC GRAPHICS

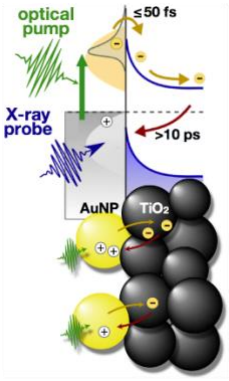

KEYWORDS: interfacial charge transfer, time-resolved X-ray photoelectron spectroscopy, plasmonic nanoparticles, photocatalysis, titanium dioxide

The conversion of solar energy into chemical fuels via photoelectrochemical (PEC) splitting of water into hydrogen and oxygen is an important component of strategies to achieve a carbon-neutral economy.[1] Heterogeneous systems consisting of plasmonic metal nanoparticles (NPs) attached to wide band gap semiconductor (SC) materials have been identified as a promising approach for renewable energy technologies based on PEC operating principles. The heterogeneous design enables increased light absorption, enhanced charge carrier separation and higher photocatalytic reactivity compared to bare wide band gap materials.[2]

The canonic model for plasmon-enabled charge generation processes at NP-SC interfaces is based on light absorption via localized surface plasmon resonances (LSPR), followed by ultrafast plasmon damping and dephasing, resulting in the population of hot electrons that are able to transfer to the SC conduction band (Fig. 1a).[3–5] Variations of this mechanism including, for example, plasmon-enabled interfacial charge-transfer excitations have been proposed as well.[6,7] Despite substantial efforts to develop plasmonic light-harvesting devices, overall device efficiencies remain quite low with most groups reporting external quantum efficiencies well below one percent[8–12] and only a few reaching higher values of a few percent.[13,14] The underlying physical limitations are not well understood and may include low charge injection efficiencies as well as challenges associated with light absorption, charge transport, back electron transfer or low yields of the catalytic reaction at the SC-liquid interface. Disentangling these individual restrictions remains challenging. In particular, the determination of NP-SC charge injection and back electron transfer rates requires time domain techniques that, ideally, are sensitive to short-lived, local charge densities. Time-resolved studies in the visible and infrared (IR) regimes monitor spatially averaged, free charge carrier densities in the SC acceptor,[3,15–17] and have led to photon-to-electron injection efficiency estimates of up to 50%.[6,15,17,18] Theoretical predictions,

however, vary only between a few[6] and up to 20%[19], and the root causes for the discrepancies between theory and experiment have yet to be identified. New techniques are sought that can provide a direct, quantitative measure of the time-dependent amount of charge inside the plasmonic NPs as well as the transient charge- and energy-distributions within the immediate, nanometer scale interfacial region between and the NPs and the SC.[20]

Here, we apply picosecond time-resolved X-ray photoelectron spectroscopy (TRXPS) to gain a site-specific perspective on photoinduced charge-transfer dynamics at the interface between spherical gold NPs (20 nm diameter) and a nanoporous TiO_2 substrate. The results provide an absolute measure of the amount of charge injected from the AuNPs into the SC substrate, indicating that ~2 electrons are transferred per NP, corresponding to a photon-to-charge conversion efficiency of ~0.1 %. Electron-hole recombination is completed within ~1 ns. The study provides the first reference-free, quantitative, microscopic, real-time insight into the efficiency and temporal evolution of charge transfer dynamics in a standard nanoplasmonic heterostructure. It demonstrates that currently available benchmark values for the first steps of photon-to-charge conversion in AuNP-sensitized TiO_2 need to be re-evaluated based on newly available data and corresponding theoretical estimates. The observations also bear consequences for the design of more efficient nanoplasmonic solar light harvesting devices as discussed below.

In the TRXPS experiment, interfacial charge-transfer dynamics are initiated by 10 ps long optical (532 nm) pump pulses and probed site-specifically at both the electron donor (AuNP) and acceptor (TiO_2) by transient changes in the Au4f and Ti2p photolines, respectively. The measurements are performed at Beamline 11.0.2 of the Advanced Light Source (ALS), using 70 ps long X-ray pulses with photon energies of $h\nu$=687 eV for the Au4f and $h\nu$=950 eV for the

Ti2p lines (see Supporting Information for further details on sample preparation and the TRXPS experiment).

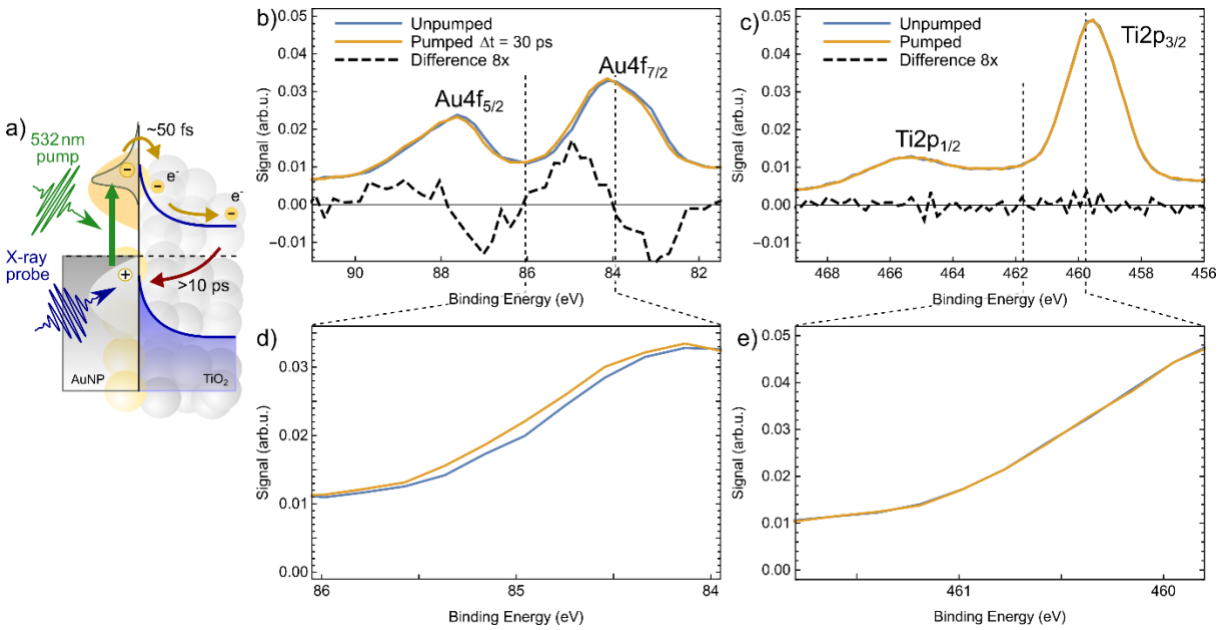

Figure 1. a) Illustration of the optical pump / X-ray-probe experiment with relevant processes and timescales at the AuNP – TiO_2 interface. (b,c) TRXPS spectra of AuNP sensitized, nanoporous films of TiO_2: Comparison of the Au4f (b) and Ti2p (c) photolines before optical excitation (blue) and at a pump-probe delay of Δt=30 ps (orange). The dashed black lines indicate the differences between the excited and ground state spectra, multiplied by a factor of 8 for better visibility. Panels d) and e) show magnified views of selected spectral ranges as indicated.

Figure 1b,c shows TRXPS spectra of the Au4f (b) and Ti2p (c) signals before laser excitation (blue) and at a pump-probe delay of Δt=30 ps (orange) for a pump-laser fluence of 0.2 mJ/cm2. The Au4f spectrum consists of the $Au4f_{5/2}$ and $Au4f_{7/2}$ peaks at 87.7 eV and 84.0 eV binding energy, respectively.[21] The Ti2p spectrum is composed of the Ti $2p_{1/2}$ and Ti $2p_{3/2}$ spin-orbit components with binding energies of 465.3 and 459.4 eV, respectively.[22] The black dashed curves correspond to the differences between the excited and the ground state spectra, multiplied by a factor of 8 for better visibility. No spectral change is observed in the Ti2p spectrum upon pump laser interaction within the signal-to-noise of the measurement. In contrast, the Au4f

spectrum exhibits a distinct response to laser excitation, leading to a bipolar structure in the difference curve for each spin-orbit component. To achieve a large acceptance solid angle for photoelectrons, an electrostatic lens system is used that leads to peak broadening but does not affect the measured shifts. The laser-induced XPS response is modeled by a rigid shift of the entire spectrum to higher binding energies. The extent of this shift is determined to ~80 meV by minimizing the difference between the neutral ground state spectrum and a shifted version of the spectrum recorded after laser excitation. In order to exclude any effects arising solely from the AuNPs, additional reference measurements are conducted that monitor the Au4f and Al2p TRXPS spectra of AuNPs deposited on Al_2O_3 substrates. In this configuration, Al_2O_3 inhibits charge transfer at the NP-SC interface, enabling the investigation of the isolated AuNP response. No photoresponse is detected in either the Au4f or the Al2p photolines of the AuNP-Al_2O_3 control samples, confirming that the transient Au4f photoresponse of the AuNP-TiO_2 samples arises from electron injection from the AuNPs into the TiO_2 substrate (see Supporting Information for details).

Time-dependent shifts of the Au4f and Ti2p spectra as a function of pump-probe delay are derived using the spectral difference minimization procedure described above, leading to the red and green markers, respectively, in Fig. 2. The laser pulse precedes the X-ray pulse for positive delays. Positive energy shifts indicate spectra with higher binding energies after laser exposure compared to the neutral ground state spectra before the pump pulse arrives.

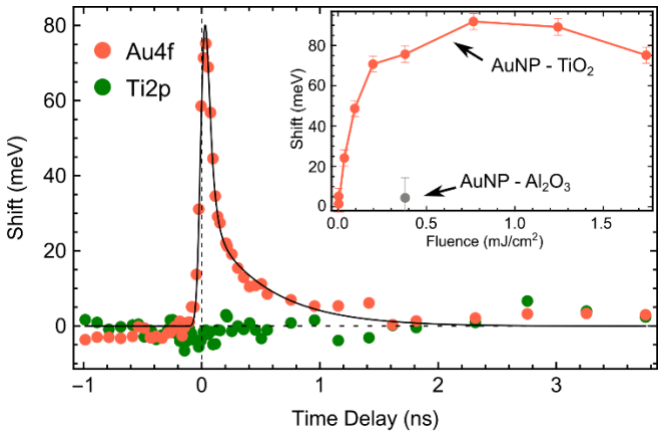

Figure 2. Site-specific, time-dependent photoresponse of the AuNP – TiO_2 interface at a pump laser fluence of 0.2 mJ/cm2. Positive shifts correspond to higher binding energies after laser excitation compared to the ground state spectra. The Au4f photoresponse is described by a bi-exponential fit model convoluted with the IRF (solid line). The fit indicates an initial decay within τ_1=60±10 ps followed by slower signal fading on a timescale of τ_2=0.8±0.2 ns. The inset shows the fluence-dependence of the maximum Au4f photoresponse at Δt=30 ps for the TiO_2 substrate (red) and the Al_2O_3 reference substrate (gray).

While the Ti2p peak is essentially unaffected by the optical excitation across all time delays, the Au4f line exhibits a pronounced response that is maximal at ~30 ps delay and subsequently decays with the involvement of multiple timescales. The trend is modeled using the following bi-exponential fit function that includes a convolution with the instrument response function (IRF):

$$\Delta BE(t) = \left(A_1 \cdot e^{-t/\tau_1} + A_2 \cdot e^{-t/\tau_2}\right) * IRF \qquad (1)$$

The amplitudes A_1 and A_2 as well as the decay constants τ_1 and τ_2 are free fit parameters, while the IRF and time zero of the time-delay axis are fixed to the results of the IRF calibration measurements (see SI). The best fit, shown as a solid curve in Fig. 2, is in good agreement with the data and indicates that the response initially decays within τ_1=60±10 ps and vanishes on a characteristic timescale of τ_2=0.8±0.2 ns. Within this description, the actual maximum amplitude of the response is given by $A_1 + A_2$ = 200±30 meV (A_1=160±30 meV, A_2=40±10 meV). In the measurement, this amplitude is reduced to ~80 meV by the IRF.

The observed amplitude of the Au4f photoresponse at 30 ps delay is further investigated as a function of pump pulse fluence as illustrated in the inset of Fig. 2. The measurement reveals a nearly linear correlation between line shift and excitation fluence up to ≈0.2 mJ/cm$_2$, beyond which the observed response saturates at approximately 80 meV. In comparison, the control experiment on AuNP - Al_2O_3 (gray dot) at a fluence of about 0.4 mJ/cm$_2$ does not indicate any measurable photoresponse.

Plasmon-induced hot-electron transfer (HET) is the most prominently discussed charge transfer mechanism for nanoplasmonic light harvesting systems. It is based on the excitation and subsequent decoherence of a surface plasmon resonance, resulting in a population of hot electrons that are able to undergo ultrafast transfer to the SC (Fig. 1a). A direct, unambiguous proof for this picture is still outstanding. Being able to quantify the amount of charge that may be extracted after absorption of *n* photons in a plasmonic light absorber is essential in order to test this and alternative physical pictures. The observed transient photoresponse presented here gives direct, quantitative insight into the electron injection efficiency per NP and the subsequent electron-hole recombination dynamics as discussed in the following.

Electron transfer from the AuNP into TiO_2 will effectively lead to a positively charged metal sphere with the excess positive charge mainly residing at the NP surface. Within this picture, the missing charge creates an additional constant potential throughout the NP, leading to an increase in the effective binding energies of the Au4f core levels, as observed in the experiment. A theoretical model is needed to translate the measured core level shifts into the amount of NP valence charges created by the NP-SC charge transfer. A first-principles based, quantitative prediction of the AuNP core binding energies as a function of the number of transferred charges is rather challenging. Instead, we use a semiclassical jellium model to estimate the valence charge distribution within

the spherical metal clusters and its impact on the Au4f photoelectron kinetic energies.[23] Within the jellium model, the positive ion cores are represented by a uniform positive background charge density.[24,25] The model predicts that excess or missing charge is accumulated within a surface layer with a width given by the Wigner-Seitz radius (R_{Wigner} = 0.165 nm for Au[26]), whereas the electron density inside the sphere stays largely unaffected. Fig. 3a schematically illustrates the electron density change for a positively charged sphere (blue solid line). The missing charge Q at the surface of the sphere with radius R_{sp}=10 nm creates a constant potential $V_Q = - Q/(4\pi\varepsilon_0 R_{sp})$ for all electrons inside the sphere and, thus, shifts their effective binding energies accordingly. Outside the sphere, the Coulomb potential decreases with 1/r, with r being the distance to the center of the sphere. The magnitude of the Coulomb potential can be considered constant throughout the XPS probing volume (see Fig. 3a, green line), which greatly simplifies the estimate of the induced shifts. The model predicts a linear dependence between observed binding energy shifts and the number of electrons injected into the SC. This is illustrated in Fig. 3b, which shows the predicted XPS peak shifts as a function of elementary charges removed from spherical AuNPs with various radii R_{SP} as indicated.

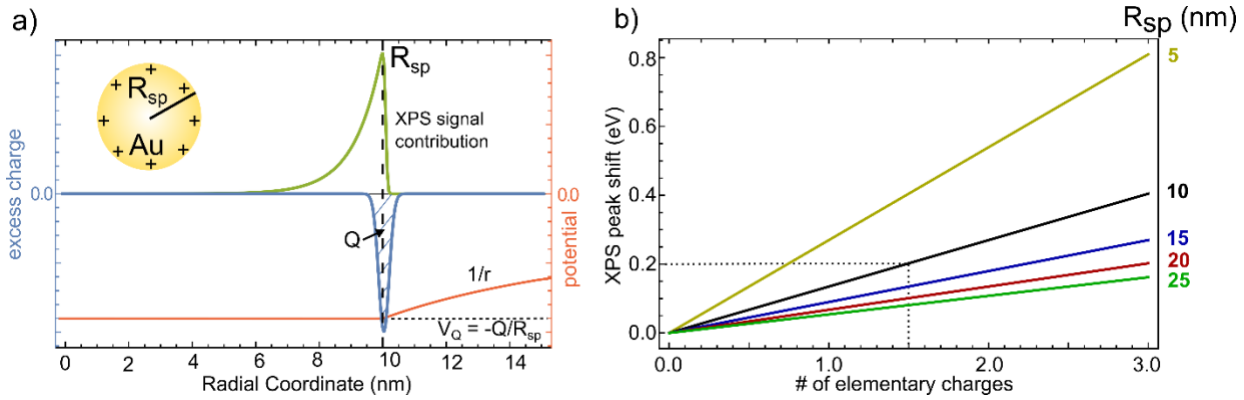

Figure 3. (a) Schematic of the electron density change (blue, left axis) induced by charge transfer from the AuNP into TiO_2 and the resulting effective potential (red, right axis) as a function of the radial coordinate measured from the center of the AuNP with a radius of R_{SP}=10 nm. The green curve represents relative XPS signal contributions based on the electron mean free path in gold. (b) Calculated XPS peak shifts as a function of the number of elementary charges on AuNPs with different radii R_{SP} as indicated. The dotted gray lines indicate the reconstructed maximum peak shift from the TRXPS measurement and the corresponding charge on the NPs used in this experiment.

Within this semiclassical approach, the reconstructed 200 meV Au4f binding energy shift obtained at a pump fluence of 0.2 mJ/cm_2 corresponds to injection of approximately 2 electrons per NP, assuming that all NPs within the probe volume contribute equally to the signal (gray dotted lines in Fig. 3b). This assumption is supported by the saturation of the photoresponse beyond 0.2 mJ/cm_2 as illustrated in the inset of Fig. 2. We note that the noise level of the measurement is on the order of ~5 meV. Requiring a measurable signal to be at least twice as large (~10 meV), this translates into a sensitivity of 1 electron leaving a AuNP with 300 nm diameter containing ~10_9 atoms.

The saturation fluence of 0.2 mJ/cm_2 corresponds to the absorption of approximately 2000 photons per AuNP based on their extinction coefficient of 9.2x10_8 $M_{-1}cm_{-1}$.[27] Correspondingly, the electron injection efficiency for this particular system, i.e., the number of injected electrons per absorbed photons, is on the order of 0.1%. This injection yield is significantly lower than those reported in several previous experimental investigations on hot charge carrier transfer in comparable systems. Estimates based on time-resolved optical absorption measurements range

from several hundred to several thousand electrons per NP of about half the size used here.[15,17,18] The substantial orders of magnitudes difference between the findings requires some attention. In particular, for time-resolved experiments utilizing short laser pulses / high peak fluences, the Coulomb potentials of the charged NP set boundaries to the maximum achievable injection efficiency both in terms of the energy that is required to overcome them as well as the maximum positive charge that may be supported by a NP without disintegration. The charge per NP measured here lies well within these energy and damage boundaries. A more detailed discussion of these aspects is provided in the Supporting Information. The measurement reveals a nearly linear correlation between line shift and excitation fluence up to ~0.2 mJ/cm$_2$, beyond which the observed response saturates at approximately 80 meV. A more detailed discussion of this trend is also provided in the SI.

The recovery of the Au4f ground state spectrum with a bi-exponential trend involving a fast 60±10 ps component and a slower 0.8±0.2 ns component reflects the back-electron transfer dynamics between the TiO_2 substrate and the AuNPs. The fast decay timescale observed here is in agreement with the findings of previous infrared (IR) transient absorption studies, which reported 1/e signal decays within ~20-100 ps.[15,18] It was shown that the TiO_2 particle size and sample preparation methods play an important role with regard to the overall lifetime.[18] Much faster initial signal decay within only 2ps was found for AuNPs fully embedded in ALD prepared TiO_2 films.[17] The observation of a significantly smaller charge carrier lifetime may arise from the different sample morphologies and/or could also be related to the different delay ranges and temporal resolution of the experiments.

The dominant sub-ns recombination timescales reported here and elsewhere may indicate a fundamental issue of the AuNP-TiO_2 system with respect to the achievable external photon-to-

current quantum yields. The electron diffusion coefficient D of TiO_2 films lies in a range of ~10^{-8} cm^2/s to ~10^{-5} cm^2/s.[28,29] Using the upper limit of D and a maximum lifetime of ~1 ns, the corresponding maximum diffusion length $L = \sqrt{D\tau}$ can be estimated to be on the order of ~1 nm. This is orders of magnitude smaller than, for example, diffusion lengths in dye-sensitized TiO_2 systems,[30,31] and indicates that efficient external charge extraction from a NP-TiO_2 heterojunction requires extremely thin SC domains.

Photoinduced charge transfer at the AuNP-TiO_2 interface results either in the generation of mobile charge carriers in the SC conduction band or the filling of trap states at the SC surface. Thus, transient spectral signatures with trends similar to those of the Au4f lines may also be expected in the Ti2p photolines. However, as can be seen in Fig. 1c, the ground and excited state spectra are indistinguishable within the experimental signal to noise ratio. Note that the missing Ti2p photoresponse cannot be associated with a lack of interfacial charge transfer in the AuNP-Ti2p system. The control experiment with the AuNP - Al_2O_3 sample confirms that the response of the Au4f lines in the AuNP – TiO_2 sample is due to photo-induced electron transfer. Therefore, the striking differences between the trends in the Au4f and Ti2p signals must be rooted in the different impacts of transient carrier densities in the donor and acceptor materials on their respective TRXPS signals. As discussed in more detail in the Supporting Information, we tentatively assign the missing Ti2p photoresponse to ultrafast surface-to-bulk diffusion of injected charges. Small total charge yields as well as the fact that the injected electron diffusion length is small compared to the AuNP size, leading to a "shadowing" effect that shields the injected electrons from detection, may also contribute.

The study illustrates the power of time-resolved X-ray photoelectron spectroscopy to investigate photoinduced charge transfer dynamics at interfaces between plasmonic NPs and nanoporous SC

substrates. The element-specificity of TRXPS allows to monitor transient, local charge distributions selectively from the perspectives of the electron donor (AuNP), complementing previous time resolved studies in the visible to IR regime. The transient increase of the effective Au4f binding energies provides a quantitative measure of the interfacial charge injection efficiency as well as the electron back transfer rate with a sensitivity of approximately one charge per 10_9 atoms. The observed photon-to-charge conversion efficiency of ~0.1% is significantly lower than values reported in some other studies but well within upper bounds set by theoretical predictions, fundamental energy conservation considerations, and target damage limits. The observed injection and electron-hole recombination dynamics provide important benchmarks for the design of plasmonic light harvesting systems. Future campaigns will investigate how the performance of the NP-SC interfaces correlates with parameters such as NP and SC materials and morphologies. Ultimately, the high sensitivity of TRXPS to transient local charges on a single electron level may enable the site-specific real-time monitoring of photoinduced chemical transformations enabled by heterogeneous nanoplasmonic assemblies.

Supporting Information. Sample preparation, Time-resolved XPS experiment and reproducibility, UV-VIS absorption spectra, Scanning electron microscopy (SEM), Control experiment with Al_2O_3 substrate, Rayleigh stability limit and total static potential energy, Fluence dependence of Au4f line shift, Photoresponse at the Ti2p edge
This material is available free of charge via the Internet

AUTHOR INFORMATION

corresponding author: ogessner@lbl.gov

Notes

The authors declare no competing financial interests.

ACKNOWLEDGMENT

This work was supported by the Atomic, Molecular, and Optical Sciences (M.Bo., J.M., F.B., O.G.) and Condensed Phase and Interfacial Molecular Science (M.Bl.) Programs of the U.S. Department of Energy, Office of Science, Office of Basic Energy Sciences, Chemical Sciences, Geosciences and Biosciences Division, through Contract No. DE-AC02-05CH11231. G.L. and F.M.T. are supported by the Joint Center for Artificial Photosynthesis, a DOE Energy Innovation Hub, supported through the Office of Science of the U.S. Department of Energy under Award Number DE-SC0004993. M.Bo, J.M., F.R., L.W., F.B., M.Bl. conducted the TRXPS experiments, M.Bo. and O.G. performed the data analysis and provided the scientific guidance, G.L., F.M.T., K.S. carried out the sample characterization by UV-vis and SEM and parts of the sample synthesis, and all authors contributed to the writing of the manuscript. The research used resources of the Advanced Light Source, a DOE Office of Science User Facility under contract no. DE-AC02-05CH11231. M.Bo. acknowledges support by the Alexander von Humboldt foundation.

REFERENCES

(1) Walter, M. G.; Warren, E. L.; McKone, J. R.; Boettcher, S. W.; Mi, Q.; Santori, E. A.; Lewis, N. S. Solar Water Splitting Cells. *Chem. Rev.* **2010**, *110*, 6446–6473, DOI:10.1021/cr1002326.

(2) Linic, S.; Christopher, P.; Ingram, D. B. Plasmonic-Metal Nanostructures for Efficient Conversion of Solar to Chemical Energy. *Nat. Mater.* **2011**, *10*, 911–921, DOI:10.1038/nmat3151.

(3) Cushing, S. K.; Li, J.; Meng, F.; Senty, T. R.; Suri, S.; Zhi, M.; Li, M.; Bristow, A. D.; Wu, N. Photocatalytic Activity Enhanced by Plasmonic Resonant Energy Transfer from Metal to Semiconductor. *J. Am. Chem. Soc.* **2012**, *134*, 15033–15041, DOI:doi.org/10.1021/ja305603t.

(4) Zhang, X.; Chen, Y. L.; Liu, R.-S.; Tsai, D. P. Plasmonic Photocatalysis. *Rep. Prog. Phys.* **2013**, *76* , 046401, DOI:doi.org/10.1088/0034-4885/76/4/046401.

(5) Christopher, P.; Moskovits, M. Hot Charge Carrier Transmission from Plasmonic Nanostructures. *Annu. Rev. Phys. Chem.* **2017**, *68*, 379–398, DOI:10.1146/annurev-physchem-052516-044948.

(6) Wu, K.; Chen, J.; McBride, J. R.; Lian, T. Efficient Hot-Electron Transfer by a Plasmon-Induced Interfacial Charge-Transfer Transition. *Science* **2015**, *349*, 632–635, DOI:doi.org/10.1126/science.aac5443.

(7) Li, J.; Cushing, S. K.; Meng, F.; Senty, T. R.; Bristow, A. D.; Wu, N. Plasmon-Induced Resonance Energy Transfer for Solar Energy Conversion. *Nat. Photonics* **2015**, *9*, 601–607, DOI:doi.org/10.1038/nphoton.2015.142.

(8) Mubeen, S.; Lee, J.; Singh, N.; Krämer, S.; Stucky, G. D.; Moskovits, M. An Autonomous Photosynthetic Device in Which All Charge Carriers Derive from Surface Plasmons. *Nat. Nanotechnol.* **2013**, *8*, 247–251, DOI:10.1038/nnano.2013.18.

(9) DeSario, P. A.; Pietron, J. J.; DeVantier, D. E.; Brintlinger, T. H.; Stroud, R. M.; Rolison, D. R. Plasmonic Enhancement of Visible-Light Water Splitting with Au–TiO2 Composite Aerogels. *Nanoscale* **2013**, *5*, 8073–8083, DOI:10.1039/C3NR01429K.

(10) Bian, Z.; Tachikawa, T.; Zhang, P.; Fujitsuka, M.; Majima, T. Au/TiO2 Superstructure-Based Plasmonic Photocatalysts Exhibiting Efficient Charge Separation and Unprecedented Activity. *J. Am. Chem. Soc.* **2014**, *136*, 458–465, DOI:10.1021/ja410994f.

(11) Ng, C.; Cadusch, J. J.; Dligatch, S.; Roberts, A.; Davis, T. J.; Mulvaney, P.; Gómez, D. E. Hot Carrier Extraction with Plasmonic Broadband Absorbers. *ACS Nano* **2016**, *10*, 4704–4711, DOI:10.1021/acsnano.6b01108.

(12) Ahn, W.; Ratchford, D. C.; Pehrsson, P. E.; Simpkins, B. S. Surface Plasmon Polariton-Induced Hot Carrier Generation for Photocatalysis. *Nanoscale* **2017**, *9*, 3010–3022, DOI:10.1039/C6NR09280B.

(13) Tian, Y.; Tatsuma, T. Mechanisms and Applications of Plasmon-Induced Charge Separation at TiO2 Films Loaded with Gold Nanoparticles. *J. Am. Chem. Soc.* **2005**, *127*, 7632–7637, DOI:10.1021/ja042192u.

(14) Nishijima, Y.; Ueno, K.; Yokota, Y.; Murakoshi, K.; Misawa, H. Plasmon-Assisted Photocurrent Generation from Visible to Near-Infrared Wavelength Using a Au-Nanorods/TiO2 Electrode. *J. Phys. Chem. Lett.* **2010**, *1*, 2031–2036, DOI:10.1021/jz1006675.

(15) Furube, A.; Du, L.; Hara, K.; Katoh, R.; Tachiya, M. Ultrafast Plasmon-Induced Electron Transfer from Gold Nanodots into TiO 2 Nanoparticles. *J. Am. Chem. Soc.* **2007**, *129*, 14852–14853, DOI:10.1021/ja076134v.

(16) Tang, Y.; Jiang, Z.; Xing, G.; Li, A.; Kanhere, P. D.; Zhang, Y.; Sum, T. C.; Li, S.; Chen, X.; Dong, Z.; Chen, Z. Efficient Ag@AgCl Cubic Cage Photocatalysts Profit from Ultrafast Plasmon-Induced Electron Transfer Processes. *Adv. Funct. Mat.* **2013**, *23*, 2932–2940, DOI:10.1002/adfm.201203379.

(17) Ratchford, D. C.; Dunkelberger, A. D.; Vurgaftman, I.; Owrutsky, J. C.; Pehrsson, P. E. Quantification of Efficient Plasmonic Hot-Electron Injection in Gold Nanoparticle–TiO2 Films. *Nano Lett.* **2017**, *17*, 6047–6055, DOI:10.1021/acs.nanolett.7b02366.

(18) Du, L.; Furube, A.; Yamamoto, K.; Hara, K.; Katoh, R.; Tachiya, M. Plasmon-Induced Charge Separation and Recombination Dynamics in Gold−TiO2 Nanoparticle Systems: Dependence on TiO2 Particle Size. *J. Phys. Chem. C* **2009**, *113*, 6454–6462, DOI:10.1021/jp810576s.

(19) Blandre, E.; Jalas, D.; Petrov, A. Yu.; Eich, M. Limit of Efficiency of Generation of Hot Electrons in Metals and Their Injection inside a Semiconductor Using a Semiclassical Approach. *ACS Photonics* **2018**, *5*, 3613–3620, DOI:10.1021/acsphotonics.8b00473.

(20) Neppl, S.; Gessner, O. Time-Resolved X-Ray Photoelectron Spectroscopy Techniques for the Study of Interfacial Charge Dynamics. *J. Electron Spectros. Relat. Phenom.* **2015**, *200*, 64–77, DOI:10.1016/j.elspec.2015.03.002.

(21) Seah, M. P.; Gilmore, I. S.; Beamson, G. XPS: Binding Energy Calibration of Electron Spectrometers 5—Re-Evaluation of the Reference Energies. *Surf. Interface Anal.* **1998**, *26*, 642–649.

(22) Erdem, B.; Hunsicker, R. A.; Simmons, G. W.; Sudol, E. D.; Dimonie, V. L.; El-Aasser, M. S. XPS and FTIR Surface Characterization of TiO2 Particles Used in Polymer Encapsulation. *Langmuir* **2001**, *17*, 2664–2669, DOI:10.1021/la0015213.

(23) Brack, M. The Physics of Simple Metal Clusters: Self-Consistent Jellium Model and Semiclassical Approaches. *Rev. Mod. Phys.* **1993**, *65*, 677–732, DOI:10.1103/RevModPhys.65.677.

(24) Bauer, D. Modeling the Core-Hole Screening in Jellium Clusters Using Density Functional Theory. *New J. Phys.* **2012**, *14*, 055012, DOI:10.1088/1367-2630/14/5/055012.

(25) Zapata Herrera, M.; Aizpurua, J.; Kazansky, A. K.; Borisov, A. G. Plasmon Response and Electron Dynamics in Charged Metallic Nanoparticles. *Langmuir* **2016**, *32*, 2829–2840, DOI:10.1021/acs.langmuir.6b00112.

(26) Smirnov, B. M. *Clusters and Small Particles: In Gases and Plasmas*; Springer Science & Business Media, 2012.

(27) Link, S.; El-Sayed, M. A. Spectral Properties and Relaxation Dynamics of Surface Plasmon Electronic Oscillations in Gold and Silver Nanodots and Nanorods. *J. Phys. Chem. B* **1999**, *103*, 8410–8426, DOI:10.1021/jp9917648.

(28) Nakade, S.; Saito, Y.; Kubo, W.; Kitamura, T.; Wada, Y.; Yanagida, S. Influence of TiO2 Nanoparticle Size on Electron Diffusion and Recombination in Dye-Sensitized TiO2 Solar Cells. *J. Phys. Chem. B* **2003**, *107*, 8607–8611, DOI:10.1021/jp034773w.

(29) Liang, L.; Dai, S.; Hu, L.; Kong, F.; Xu, W.; Wang, K. Porosity Effects on Electron Transport in TiO2 Films and Its Application to Dye-Sensitized Solar Cells. *J. Phys. Chem. B* **2006**, *110*, 12404–12409, DOI:10.1021/jp061284y.

(30) Benkö, G.; Kallioinen, J.; Korppi-Tommola, J. E. I.; Yartsev, A. P.; Sundström, V. Photoinduced Ultrafast Dye-to-Semiconductor Electron Injection from Nonthermalized and Thermalized Donor States. *J. Am. Chem. Soc.* **2002**, *124*, 489–493, DOI:10.1021/ja016561n.
(31) Němec, H.; Rochford, J.; Taratula, O.; Galoppini, E.; Kužel, P.; Polívka, T.; Yartsev, A.; Sundström, V. Influence of the Electron-Cation Interaction on Electron Mobility in Dye-Sensitized ZnO and TiO2 Nanocrystals: A Study Using Ultrafast Terahertz Spectroscopy. *Phys. Rev. Lett.* **2010**, *104*, 197401, DOI:10.1103/PhysRevLett.104.197401.

Supporting Information

Photoinduced Charge Carrier Dynamics and Electron Injection Efficiencies in Au Nanoparticle-Sensitized TiO_2 Determined with Picosecond Time-Resolved X-ray Photoelectron Spectroscopy

Mario Borgwardt[1], Johannes Mahl[1], Friedrich Roth[2], Lukas Wenthaus[3], Felix Braußе[1], Monika Blum[1,4], Klaus Schwarzburg[5], Guiji Liu[1,6], Francesca M. Toma[1,6], and Oliver Gessner[1]*

[1]Chemical Sciences Division, Lawrence Berkeley National Laboratory, Berkeley, California 94720, USA
[2]Institute of Experimental Physics, TU Bergakademie Freiberg, D-09599 Freiberg, Germany
[3]Deutsches Elektronen Synchrotron / DESY, D-22607 Hamburg, Germany
[4]Advanced Light Source, Lawrence Berkeley National Laboratory, Berkeley, California 94720, United States
[5]Institute for Solar Fuels, Helmholtz-Zentrum Berlin für Materialien und Energie GmbH, 14109, Berlin, Germany
[6]Joint Center for Artificial Photosynthesis, Lawrence Berkeley National Laboratory, California 94720, USA

*corresponding author: ogessner@lbl.gov

S1. Sample Preparation

Nanoporous anatase TiO_2 films deposited on FTO glass (Solaronix Ti-Nanoxide T/SP, 15 - 20nm particle size) are sintered at 450°C for 30min. While the substrates are still hot (≈100°C), a suspension of gold nanoparticles (AuNPs) in water (20 nm diameter, Sigma-Aldrich) is drop-cast on the TiO_2 films and dried on a hot plate for several hours with subsequent transfer in air into the experimental vacuum chamber. The resulting AuNP/TiO_2 samples exhibit the characteristic plasmon absorption band of the Au nanoparticles (see Fig. S2). The capping agent (citrate buffer) is removed by a mild heating cycle after sample preparation[1] which was verified by XPS measurements that did not reveal any signatures of the buffer. Additionally, UV-vis absorption spectra of AuNPs deposited on a glass substrate were recorded before and after the additional heating cycle. With the buffer present, the characteristic plasmon resonance is significantly broadened and red-shifted. After the heating cycle, the expected width and position of the plasmon resonance are restored. We note that well-defined sample conditions are confirmed by the extremely good reproducibility of the TRXPS measurements for different samples and measurements presented in section S2. Control experiments are conducted using AuNP-sensitized nanoporous films of Al_2O_3, for which no charge injection is expected (see section S5). The shape and location of the AuNP plasmon resonance are very similar for all three substrates (see section S3). Surface coverage and morphology is investigated by scanning electron microscopy (SEM). SEM images suggest a NP coverage of ≤20% as shown below.

S2. Time-resolved XPS experiment and reproducibility

The time-resolved laser pump – X-ray probe experiments are performed at Beamline 11.0.2 of the Advanced Light Source (ALS). A detailed description of the TRXPS setup can be found

elsewhere.[2] Briefly, TRXPS signals are recorded with 70 ps X-ray pulses (hν=687 eV for Au4f, Al2p, hν=950 eV for Ti2p) from the ALS operated in 2-Bunch mode (~3 MHz), using a hemispherical electron analyzer equipped with a delay-line detector that simultaneously records the hit positions and arrival times of individual electrons. The excitation laser system provides 10 ps long pulses and is synchronized to the ALS pulse train. It is operated at a wavelength of 532 nm with a pulse repetition rate of ≈127 kHz. A time-stamping technique enables efficient laser-pump / multiple X-ray probe measurements. The instrument response function (IRF) with a full-width-at-half-maximum (FWHM) of 70 ps is essentially defined by the bunch length of the ALS and determined using the transient surface photovoltage response of a clean Si(100) substrate without surface oxide layer. The spot sizes of the laser pump- and X-ray probe-beams at the sample are (280x120) μm^2 and (50x50) μm^2, respectively, ensuring good pump-probe overlap and uniform excitation conditions across the probed sample area. Laser or X-ray induced sample damage is not observed for laser pump fluences below 0.5 mJ/cm^2 and, therefore, all time-resolved measurements requiring extended acquisition times were performed below this value. For power-dependent measurements with pump laser fluences exceeding the damage threshold, exposure times were limited to avoid the impact from radiation damage.

Figure S1 illustrates the excellent reproducibility of the results. It shows a comparison of dynamic trends in the Au4f photolines of two different samples recorded during two different experimental runs at the ALS synchrotron in November 2018 and November 2019 as indicated. No relative scaling has been applied to the two data sets. The results are virtually identical including the outcome of fits to eqn. (1) of the main manuscript. An initial fast τ_1=60±10 ps decay is followed by a slower signal fading on a timescale of τ_2=0.8±0.2 ns. Only the amplitude ratio varies slightly with A_1=160±30 meV, A_2=40±10 meV for the November 2018 and A_1=170±30 meV, A_2=30±10

meV for the November 2019 beamtime. Given the excellent reproducibility of the results and the standardized nature of both the raw materials and the sample preparation procedure, the results are expected to be directly comparable to other studies using the same or very similar approaches.

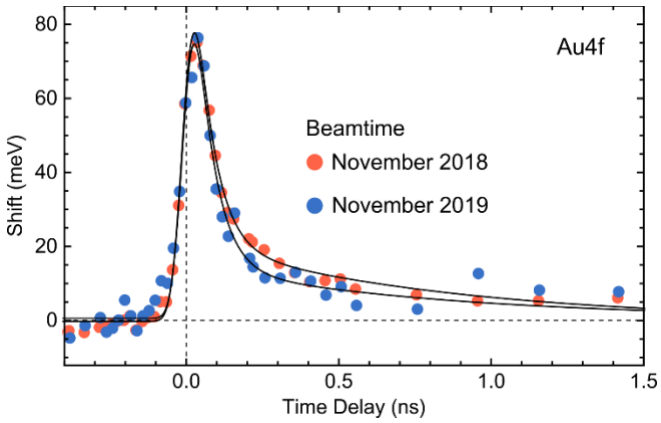

Figure S1. Comparison of the time-dependent Au4f photoresponse of two different AuNP – TiO_2 samples used during two experimental runs at the ALS, conducted one year apart as indicated. The pump laser fluence is 0.2 mJ/cm_2 in both cases. Positive shifts correspond to higher binding energies after laser excitation compared to the ground state spectra. The Au4f photoresponses are described by a bi-exponential fit model convoluted with the IRF (solid line, see eqn. (1) in main manuscript). The fit confirms that identical dynamics are observed in both experiments. No relative scaling has been applied to the two data sets.

S3. UV-VIS absorption spectra

Fig. S2 illustrates the shape and location of the AuNP plasmon resonance in the UV-vis absorption spectrum using three different substrates. AuNPs were deposited on a) a glass substrate, b) a 30 nm thick film of Al_2O_3 produced by atomic layer deposition (ALD), and c) the nanoporous TiO_2 substrate used in the experiment. As indicated by the green marker, the 532 nm wavelength of the

pump laser is very close to the maximum of the plasmon resonance in all cases, demonstrating that the plasmon excitation conditions are virtually identical for all substrates.

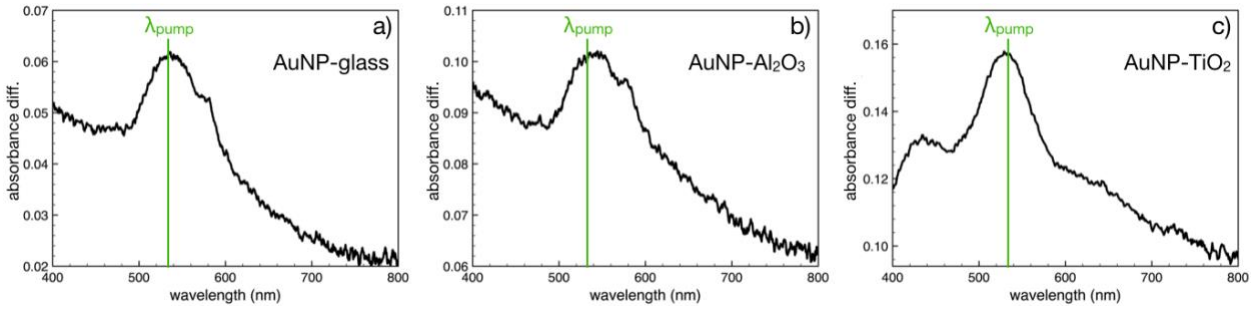

Figure S2. UV-vis absorption spectra of AuNPs deposited on a) glass, b) Al_2O_3, c) TiO_2. Shown are differences in absorbance when comparing samples with and without AuNPs deposited on the respective substrates. The green vertical lines mark the wavelength of the pump laser used in this study (532 nm).

S4. Scanning electron microscopy (SEM)

a)

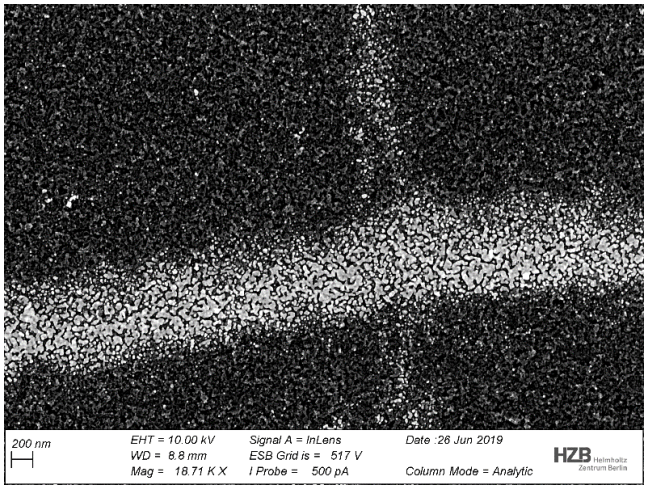

b)

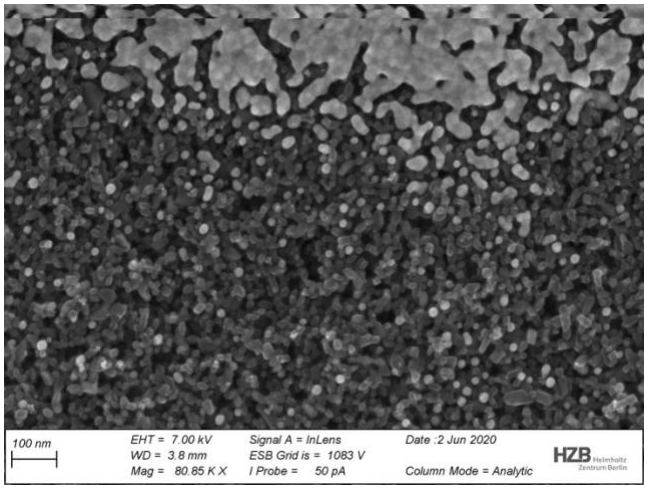

c)

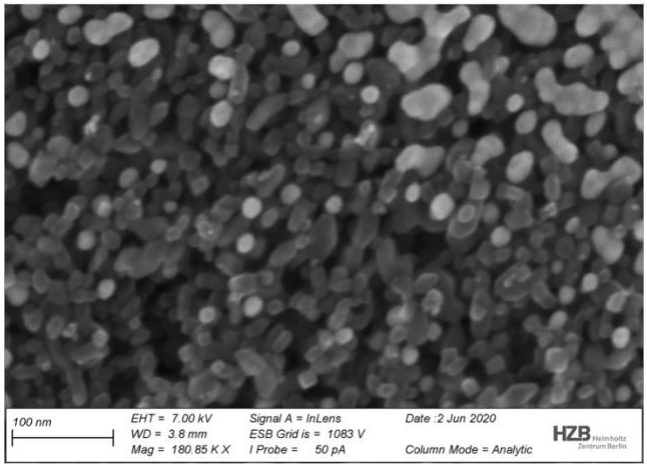

Figure S3. Representative SEM images of the AuNP-TiO_2 sample. a) Overview image indicating a surface coverage of $\lesssim$ 20%, b), c) detailed high-resolution views confirming the nanoporous morphology of the sample with a characteristic 20 nm particle size. The bright stripe in a) and the regions of islands in b) and c) are caused by a "coffee ring" effect during the deposition of the AuNPs.

S5. Control experiment with Al_2O_3 substrate

In order to exclude any effects arising solely from the AuNPs, a reference sample consisting of a AuNP-sensitized thin film of Al_2O_3 was used. Since the conduction band edge of Al_2O_3 is located 4.0 eV above that of TiO_2[3,4] no electron transfer from the AuNPs is expected and, thus, the sample can be used to monitor the isolated response of excited gold nanodots. Figure S4 shows a comparison of the Au4f photoresponses for AuNPs attached to TiO_2 (orange) and Al_2O_3 (green). Note that the absorption conditions for the 532 nm pump laser light due to the AuNP plasmon resonance are virtually identical for both substrates, as shown in Fig. S2. The missing response in the AuNP – Al_2O_3 control sample confirms that the Au4f transient shifts of the AuNP – TiO_2 sample are due to electrons injected into the TiO_2 substrate. We note, that the increased noise level for the AuNP – Al_2O_3 sample is a consequence of charging effects associated with the wide bandgap SC material, which introduce some additional variations in the photoelectron lines.

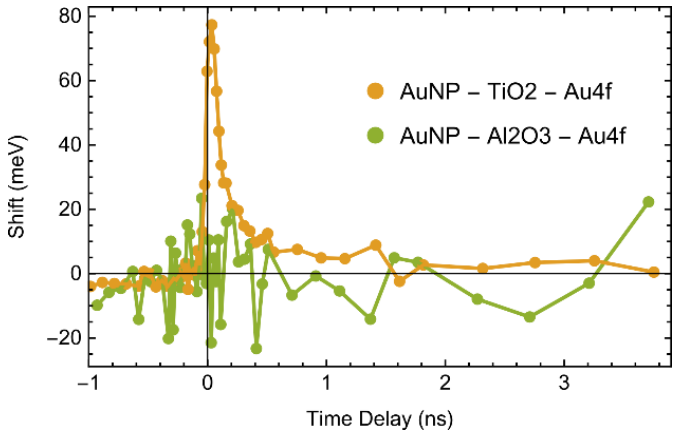

Figure S4. Time-resolved photo-response in the AuNP – TiO_2 (orange) and AuNP – Al_2O_3 control sample (green).

S6. Rayleigh stability limit and total static potential energy

An upper limit for electron injection is given by the requirement that the Coulomb repulsion forces between the holes within the NPs have to remain below their fission threshold. A basic estimate for this boundary condition is provided by the Rayleigh limit that predicts that fission in charged clusters becomes relevant if the square of the number of charges z exceed the number n of atoms in the cluster ($z^2 > n$).[5,6] For AuNPs with a radius R_{sp}=10 nm consisting of 250,000 atoms, the Rayleigh stability limit corresponds to an injection yield of 500 electrons per NP or 2×10^{-3} charges per atom[7]. Furthermore, experimental results of positively charged Na clusters suggest that the Rayleigh formula overestimates the critical number of charges so that even less charging can already induce instabilities.[8,9] Thus, injection yields beyond a few hundred electrons per NP appear to be unsustainable without damaging the sample. The injection yield derived here corresponds to ~10^{-5} charges per atom and lies almost two orders of magnitude below the Rayleigh stability limit. Based on the jellium model presented in the main text, the total energy required to remove n elementary charges from a single AuNP with radius R_{sp} into vacuum is

$$E_{tot} = e^2(n^2+n)/(8\pi\varepsilon_0 R_{sp}), \qquad (1)$$

where e is the elementary charge and ε_0 is the vacuum permittivity. Eq. (1) corresponds to the integral over the Coulomb potential as it increases with the number of removed charges. As an example, consider absorption of 2000 photons from a 532 nm excitation laser, corresponding to a total deposited energy of 4.66 keV. Even if all energy would be available to remove charges from the R_{sp}=10 nm AuNPs, the maximum number of charges would be 254, corresponding to a hypothetical photon-to-charge conversion efficiency of 12.7%. Due to the n^2 term in eq. (1), the

theoretical maximum efficiency drops with increasing number of photons and, thus, applied pump fluence. The same holds true for increasing NP size as illustrated in Fig. S5.

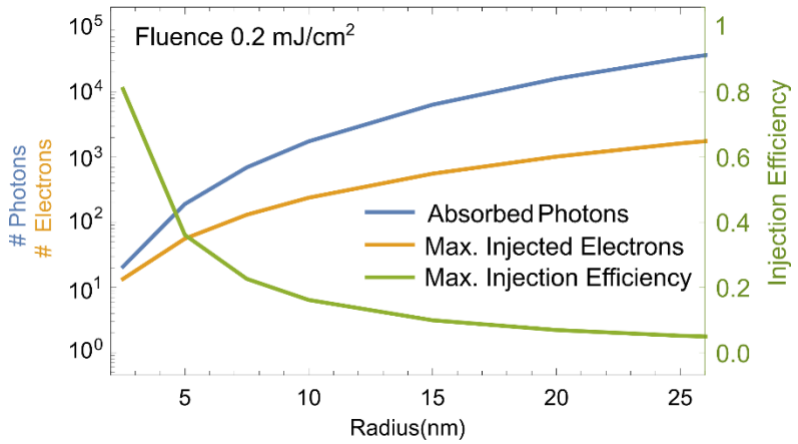

Figure S5 Maximum injection efficiency estimate for a fluence of 0.2 mJ/cm$_2$, derived from the total potential energy of electron-hole pairs in comparison to the total absorbed photon energy. Shown are the absorbed number of photons (blue, log scale left), the maximum number of injected electrons (orange, log scale left), and the maximally achievable injection efficiency (green, linear scale, right) in dependence of the NPs radius. Estimates are based on a AuNP extinction coefficient of 9.2x10$_8$ M$_{-1}$cm$_{-1}$ for 20 nm diameter NPs and an approximately linear scaling of the number of absorbed photons per NP with the NP volume..

The total number of absorbed photons scales approximately linearly with the sphere volume and thus cubically with the radius (R_{sp3}). On the other hand, for $n \gg 1$, the maximum injected charge grows quadratically with the radius (R_{sp2}), leading to a theoretical maximum injection efficiency that is inversely proportional to the sphere radius. In light of these estimates, it appears principally challenging to achieve some of the photon-to-charge conversion efficiencies reported in the literature.[10–12] For comparison, the total energy for two electrons to overcome the Coulomb potential from the AuNP used in this study is 0.43 eV. It is, however, important to note, that the above calculations are only relevant for photon fluences reached in pulsed experiments. Under cw conditions, lower current densities must be considered, most likely leading to higher overall achievable boundaries regarding these potential energy considerations.

S7. Fluence dependence of Au4f line shift

The fluence-dependence of the Au4f line shift illustrated in the inset of Fig. 2 indicates a non-trivial relationship between the number of photons incident on the gold NPs and the number of electrons injected into the TiO_2 substrate for high fluences. While a detailed discussion of this effect is beyond the scope of this work, it should be noted that saturation effects in nanoplasmonic absorbers and light-harvesting systems have previously been observed by several other groups.[13–18] Fang and co-workers[18] recently reported electron injection yields in plasmonic Au/MoS_2 heterostructures to saturate at fluences as low as ~10 μJ/cm^2 (~1.4 x 10^8 W/cm^2 peak power). The authors tentatively assign the effect to large numbers of electrons transferred to the SC blocking the injection of additional charges. The estimated charge density at saturation is 3.55 x 10^{11} cm^{-2}. Here, based on a saturated injection yield of ~2 electrons per NP and a TiO_2 surface coverage by Au NPs of ~20 % (Fig. S3), the average area density of electrons in the SC substrate at saturation is estimated to ~1.3 x 10^{11} cm^{-2}, which is on the same order of magnitude as the one previously observed. We note, however, that a direct comparison of the values is difficult. The NP surface coverage in the experiment reported here is very inhomogeneous (Fig. S3). Thus, on microscopic length scales, local charge densities may vary substantially compared to the average value given above. The different SC materials and morphologies in the two experiments may also have an impact. Nevertheless, the similarities in the orders of magnitude estimates could be linked to similar physical origins of the observed saturation effects.

Saturation of plasmon-enhanced absorption in the gold NPs could also be a contributing factor.[13–17] However, the relatively low saturation peak power observed here (~2 x 10^7 W/cm^2) in combination with the very pronounced onset of saturation at this value makes it unlikely that saturable absorption is the dominant factor. Typically, saturation effects are observed at orders of

magnitude higher peak powers using femtosecond light pulses and vary greatly with pulse length.[15] Finally, we note that sample damage effects have been excluded as a possible root cause for the saturation shown in Fig. 2 by repeatedly measuring the entire fluence-dependent line-shift curve without altering the sample position, leading to identical results within experimental uncertainties.

S8. Photoresponse at the Ti2p edge

As discussed in the main text and as can be seen in Fig. 1c,e, the ground and excited state spectra of the Ti2p photoline are indistinguishable within the signal to noise ratio. The lack of a photoresponse cannot be associated with a lack of interfacial charge transfer in the AuNP-TiO_2 system as confirmed by the control experiment with the AuNP - Al_2O_3 sample. Therefore, the striking differences between the trends in the Au4f and Ti2p signals must be rooted in the different impacts of transient carrier densities in the donor and acceptor materials on their respective TRXPS signals.

We note that a similar TRXPS experiment monitoring photoinduced charge transfer at the molecule-SC interface in a film of dye-sensitized ZnO nanocrystals revealed pronounced transient responses in photolines associated with both the dye molecules and the SC substrate[19]. Basic estimates suggest that, under common experimental conditions, a few electrons are injected into each TiO_2 or ZnO NP of a nanoporous dye-sensitized substrate, which is comparable to the situation at each single AuNP-TiO_2NP interface.[20] Thus, the TRXPS technique is principally sensitive to electronic dynamics in both the electron donor and acceptor materials for single-particle charge densities expected herein. However, the geometry and overall donor coverage of the AuNP-TiO_2 sample studied here are significantly different from the situation found in dye-sensitized nanoparticle films, leading to important differences in the SC photoresponses as discussed in the following.

The surface-to-bulk electron diffusion in TiO_2 substrates is known to be much more efficient than in ZnO substrates and, thus, may render the charges inaccessible to probing via XPS on picosecond timescales.[21] For example, Gundlach et al. used tr-2PPE with sub-100 fs resolution to study charge transfer dynamics between catechol molecules and TiO_2 NPs. It was found that most injected electrons escape from the experimentally accessible surface region within less than 10 fs.[22] Similar timescales were found by Duncan et al. by ab initio nonadiabatic molecular dynamics calculations, indicating that delocalization of electrons from the surface into the bulk proceeds on a timescale of ~100 fs.[23,24] These results suggest that the limited temporal response and high surface sensitivity of the picosecond TRXPS experiment may contribute to a restricted access to transient injected charges in the TiO_2 substrate.

Principally, long-lived surface trapped species with >10ps lifetimes could contribute to spectral changes of the Ti2p line. However, Amidani et al. estimated that for an anatase TiO_2 substrate with 15 nm particle size, covered by 5 nm AuNPs, the conversion efficiency of photons into long-lived electrons trapped at substrate surface sites is only ≈0.1%,[25] which is below the detection limit of the experiment presented here. Gaining a more comprehensive picture of the ultrafast dissipation mechanism may be possible through experiments utilizing femtosecond pump- and probe-pulses, as available at x-ray free-electron lasers (XFELs) and by a more systematic comparison of samples based on ZnO and TiO_2 substrates with varying electron donor coverages and electron kinetic energies, i.e., probing depths.

Moreover, the geometry and overall donor coverage of the AuNP-TiO_2 sample studied here are significantly different from the situation found in dye-sensitized nanoparticle films, which may also lead to important differences in the SC photoresponse. Notably, the size of the gold nanoparticles (R≈10 nm) is significantly larger than the upper bound for the electron diffusion

length in the TiO_2 substrate ($L \lesssim 1$nm) and only ≤20% of the SC substrate is covered by NPs. Additionally, the inelastic mean free path in gold for photoelectrons ejected from the substrate (IMFP<0.86nm)[26] is orders of magnitude smaller than the NP size. Thus, the AuNPs effectively block XPS access to substrate regions that are subject to electron injection and, vice versa, virtually all detected Ti2p photoelectrons are ejected from substrate sites that are unaffected by interfacial charge transfer. In addition, the sparse AuNP coverage in the experiment presented here and the injection efficiency of only a few electrons per electron donor correspond to an average number of injected electrons per substrate NP that is approximately an order of magnitude smaller than in dye-sensitized SCs.

References

(1) Imura, Y.; Furukawa, S.; Ozawa, K.; Morita-Imura, C.; Kawai, T.; Komatsu, T. Surface Clean Gold Nanoflower Obtained by Complete Removal of Capping Agents: An Active Catalyst for Alcohol Oxidation. *RSC Adv.* **2016**, *6*, 17222–17227, DOI:10.1039/C5RA27146K.

(2) Neppl, S.; Shavorskiy, A.; Zegkinoglou, I.; Fraund, M.; Slaughter, D. S.; Troy, T.; Ziemkiewicz, M. P.; Ahmed, M.; Gul, S.; Rude, B.; Zhang, J. Z.; Tremsin, A. S.; Glans, P.-A.; Liu, Y.-S.; Wu, C. H.; Guo, J.; Salmeron, M.; Bluhm, H.; Gessner, O. Capturing Interfacial Photoelectrochemical Dynamics with Picosecond Time-Resolved X-Ray Photoelectron Spectroscopy. *Faraday Discuss.* **2014**, *171*, 219–241, DOI:10.1039/C4FD00036F.

(3) Palomares, E.; Clifford, J. N.; Haque, S. A.; Lutz, T.; Durrant, J. R. Control of Charge Recombination Dynamics in Dye Sensitized Solar Cells by the Use of Conformally Deposited Metal Oxide Blocking Layers. *J. Am. Chem. Soc.* **2003**, *125*, 475–482, DOI:10.1021/ja027945w.

(4) Afanas'ev, V. V.; Houssa, M.; Stesmans, A.; Heyns, M. M. Band Alignments in Metal–Oxide–Silicon Structures with Atomic-Layer Deposited Al_2O_3 and ZrO_2. *J. Appl. Phys.* **2002**, *91*, 3079–3084, DOI:10.1063/1.1436299.

(5) Saunders, W. A. Fission and Liquid-Drop Behavior of Charged Gold Clusters. *Phys. Rev. Lett.* **1990**, *64*, 3046–3049, DOI:10.1103/PhysRevLett.64.3046.

(6) Näher, U.; Bjørnholm, S.; Frauendorf, S.; Garcias, F.; Guet, C. Fission of Metal Clusters. *Phys. Rep.* **1997**, *285*, 245–320, DOI:10.1016/S0370-1573(96)00040-3.

(7) Näher, U.; Frank, S.; Malinowski, N.; Zimmermann, U.; Martin, T. P. Fission of Highly Charged Alkali Metal Clusters. In *Atomic and Nuclear Clusters*; Anagnostatos, G. S., von Oertzen, W., Eds.; Springer Berlin Heidelberg, 1995; pp 102–108.
(8) Näher, U.; Göhlich, H.; Lange, T.; Martin, T. P. Observation of Highly Charged Sodium Clusters. *Phys. Rev. Lett.* **1992**, *68*, 3416–3419, DOI:10.1103/PhysRevLett.68.3416.
(9) Vasyutin, E. V.; Pogosov, V. V. Coulomb Instability of Charged Clusters. *Phys. Solid State* **2004**, *46*, 1927–1932, DOI:10.1134/1.1809433.
(10) Furube, A.; Du, L.; Hara, K.; Katoh, R.; Tachiya, M. Ultrafast Plasmon-Induced Electron Transfer from Gold Nanodots into TiO_2 Nanoparticles. *J. Am. Chem. Soc.* **2007**, *129*, 14852–14853, DOI:10.1021/ja076134v.
(11) Ratchford, D. C.; Dunkelberger, A. D.; Vurgaftman, I.; Owrutsky, J. C.; Pehrsson, P. E. Quantification of Efficient Plasmonic Hot-Electron Injection in Gold Nanoparticle–TiO_2 Films. *Nano Lett.* **2017**, *17*, 6047–6055, DOI:10.1021/acs.nanolett.7b02366.
(12) Du, L.; Furube, A.; Yamamoto, K.; Hara, K.; Katoh, R.; Tachiya, M. Plasmon-Induced Charge Separation and Recombination Dynamics in Gold−TiO_2 Nanoparticle Systems: Dependence on TiO_2 Particle Size. *J. Phys. Chem. C* **2009**, *113*, 6454–6462, DOI:10.1021/jp810576s.
(13) Ahmadi, T. S.; Logunov, S. L.; El-Sayed, M. A. Picosecond Dynamics of Colloidal Gold Nanoparticles. *J. Phys. Chem.* **1996**, *100*, 8053–8056, DOI:10.1021/jp960484e.
(14) Elim, H. I.; Yang, J.; Lee, J.-Y.; Mi, J.; Ji, W. Observation of Saturable and Reverse-Saturable Absorption at Longitudinal Surface Plasmon Resonance in Gold Nanorods. *Appl. Phys. Lett.* **2006**, *88*, 083107, DOI:10.1063/1.2177366.
(15) Ros, I.; Schiavuta, P.; Bello, V.; Mattei, G.; Bozio, R. Femtosecond Nonlinear Absorption of Gold Nanoshells at Surface Plasmon Resonance. *Phys. Chem. Chem. Phys.* **2010**, *12*, 13692–13698, DOI:10.1039/C0CP00783H.
(16) Gao, Y.; Zhang, X.; Li, Y.; Liu, H.; Wang, Y.; Chang, Q.; Jiao, W.; Song, Y. Saturable Absorption and Reverse Saturable Absorption in Platinum Nanoparticles. *Opt. Commun.* **2005**, *251*, 429–433, DOI:10.1016/j.optcom.2005.03.003.
(17) Silva, M. G.; Teles-Ferreira, D. C.; Siman, L.; Chaves, C. R.; Ladeira, L. O.; Longhi, S.; Cerullo, G.; Manzoni, C.; de Paula, A. M.; Della Valle, G. Universal Saturation Behavior in the Transient Optical Response of Plasmonic Structures. *Phys. Rev. B* **2018**, *98*, 115407, DOI:10.1103/PhysRevB.98.115407.
(18) Shan, H.; Yu, Y.; Wang, X.; Luo, Y.; Zu, S.; Du, B.; Han, T.; Li, B.; Li, Y.; Wu, J.; Lin, F.; Shi, K.; Tay, B. K.; Liu, Z.; Zhu, X.; Fang, Z. Direct Observation of Ultrafast Plasmonic Hot Electron Transfer in the Strong Coupling Regime. *Light Sci. Appl.* **2019**, *8*, 1–9, DOI:10.1038/s41377-019-0121-6.
(19) Mahl, J.; Neppl, S.; Roth, F.; Shavorskiy, A.; Huse, N.; Bluhm, H.; Eberhardt, W.; Gessner, O. Real-Time Probing of Charge-Transfer Induced Interfacial Fields in a Dye-Semiconductor System Using Time-Resolved XPS. *EPJ Web Conf.* **2019**, *205*, 05021, DOI:10.1051/epjconf/201920505021.
(20) Hao, E.; Anderson, N. A.; Asbury, J. B.; Lian, T. Effect of Trap States on Interfacial Electron Transfer between Molecular Absorbates and Semiconductor Nanoparticles. *J. Phys. Chem. B* **2002**, *106*, 10191–10198, DOI:10.1021/jp021226m.
(21) Němec, H.; Rochford, J.; Taratula, O.; Galoppini, E.; Kužel, P.; Polívka, T.; Yartsev, A.; Sundström, V. Influence of the Electron-Cation Interaction on Electron Mobility in Dye-

Sensitized ZnO and TiO_2 Nanocrystals: A Study Using Ultrafast Terahertz Spectroscopy. *Phys. Rev. Lett.* **2010**, *104*, 197401, DOI:10.1103/PhysRevLett.104.197401.
(22) Gundlach, L.; Ernstorfer, R.; Willig, F. Escape Dynamics of Photoexcited Electrons at Catechol : TiO_2(110). *Phys. Rev. B* **2006**, *74*, 035324, DOI:10.1103/PhysRevB.74.035324.
(23) Duncan, W. R.; Stier, W. M.; Prezhdo, O. V. Ab Initio Nonadiabatic Molecular Dynamics of the Ultrafast Electron Injection across the Alizarin−TiO_2 Interface. *J. Am. Chem. Soc.* **2005**, *127*, 7941–7951, DOI:10.1021/ja042156v.
(24) Duncan, W. R.; Prezhdo, O. V. Theoretical Studies of Photoinduced Electron Transfer in Dye-Sensitized TiO_2. *Annu. Rev. Phys. Chem.* **2007**, *58*, 143–184, DOI:10.1146/annurev.physchem.58.052306.144054.
(25) Amidani, L.; Naldoni, A.; Malvestuto, M.; Marelli, M.; Glatzel, P.; Dal Santo, V.; Boscherini, F. Probing Long-Lived Plasmonic-Generated Charges in TiO_2/Au by High-Resolution X-Ray Absorption Spectroscopy. *Angew. Chem. Int. Ed.* **2015**, *54*, 5413–5416, DOI:10.1002/anie.201412030.
(26) Tanuma, S.; Powell, C. J.; Penn, D. R. Calculations of Electron Inelastic Mean Free Paths. *Surf. Interface Anal.* **2005,** *37*, 1–14, DOI:10.1002/sia.1997.